Steady streaming flow induced by active biological microstructures; application to small intestine villi

Midhun Puthumana Melepattu, Clément de Loubens

Steady streaming flow induced by active biological microstructures; application to small intestine villi

Midhun Puthumana Melepattu[1] and Clément de Loubens[1, a)]
Univ. Grenoble Alpes, CNRS, Grenoble INP, LRP, 38000 Grenoble, France

(Dated: 9 May 2022)

Physiological transport of fluid at small scales is often achieved by microscopic active finger-like structures. It is recognized that they have to move in a non-symmetric fashion in order to break the symmetry of creeping flow and to induce a net movement of the fluid. However, in the limit of low, but non-vanishing, Reynolds number, irreversible flow on long time scales could also be generated by symmetric oscillations of these microstructures.

Inspired by small intestine villi, we reported three dimensional direct numerical simulations of the irreversible part of the flow, namely steady streaming flow (SSF), generated by an array of oscillating finger-like structures. In order to capture these second order flow phenomena, the algorithm was based on a combination of lattice-Boltzmann methods with two relaxation times and the smoothed profile method.

SSF was confined inside a steady viscous boundary above the villi. Two steady vortices at the tip of the villi characterized this flow, which induced mass transfers between the bulk and the periphery. Strikingly, the spatial extension of these vortices was not solely governed by the Stokes boundary layer but also by the lateral confinement between the villi. Moreover, secondary vortices outside the steady boundary layer were also observed. These findings were rationalized in a state diagram showing three regimes of SSF. Lastly, orders of magnitude showed that SSF should contribute to the transport of particles, such as bacteria or nano-particles, on a layer of a few hundred micrometers above the villi and on time scales of few minutes.

I. INTRODUCTION

Transport of fluids at small scale in biological organisms is achieved by active boundaries or active microstructures. The main constraint is coping with the strong dominance of viscous force over inertia which means that any reversible movement of these boundaries or structures does not induce a net movement of the fluid.[2,3] In the lymphatic vessels, microscopic valves prevent the reflux of lymph during the contraction of lymphangions.[4] In the airways, the cerebral ventricles or the female reproductive tract, propulsion is achieved by carpets of ciliated cells, which are microscopic, active and flexible finger-like structures of a few dozen micrometers in length.[5] Net movement of the fluid in one direction is made possible with the non-reciprocal beating of these cilia and their coordination.[6–10]

In the gastrointestinal tract, flow and mixing is secured at macroscopic scale by smooth muscle motility which generates standing and propagating contractions (e.g. segmentation and peristaltis).[11,12] Like other organs, small intestine mucosa is also covered by finger-shaped or leaf-shaped microstructure of a few hundred micrometers in length called villi (Fig. 1-a). Whereas it has long been considered that the presence of villi should passively increase the absorption of nutrients by increasing the exchange surface between the mucosa and the lumen,[13] several studies have pointed out an active enhancement of absorption by these structures.[14–16] At first sight, this enhancement could be explained by the observations of Gruby and Delafond in 1843,[17] who reported spontaneous activity of villi in living animals. Uncoordinated piston-like and pendular movements of villi were described one century later in *ex-vivo* preparations.[18–21] More recently, characterization of the mechanical behaviour of isolated villi under flow showed that villi can be considered as relatively rigid structures that cannot be deformed by physiological flow[22] and their movement is driven by standing or propagating activity of the mucosa.[1] It is very unlikely that net fluid transport in the small intestine at microscopic scale is induced by a non-symmetric motion of villi motion, contrary to flexible ciliated cells. Consequently, in creeping flow conditions, the only source of irreversibility in mass transfers generated by symmetric activity of the villi is diffusion.[1,23,24] However, it is worth noting that there is a difference of several orders of magnitudes between the time scale of smooth muscle motility (~ 1 s) and the resident time of the fluid in the small intestine ($\sim 10^3$ s).[25] These considerations lead us to the hypothesis that cyclic and symmetric movement of the villi could trigger second order flow phenomena, at low, but non vanishing, Reynolds number, and consequently irreversible transport phenomena on long time scales.

Indeed, periodic forcing flow at moderate Reynolds number induced a non-zero time average flow, the so-called steady-streaming flow (SSF).[26] This flow phenomena can be triggered by an acoustic wave,[27] a periodic pressure gradient,[28] or the oscillation of a rigid body.[29] SSF results from the time-irreversible convective term in Navier-Stokes equations and attracts lots of attention to overcome limitations of low Reynolds number flows for active mixing, particle sorting in microfluidics devices[27,30,31] or trapping particles with hy-

a)clement.de-loubens@univ-grenoble-alpes.fr

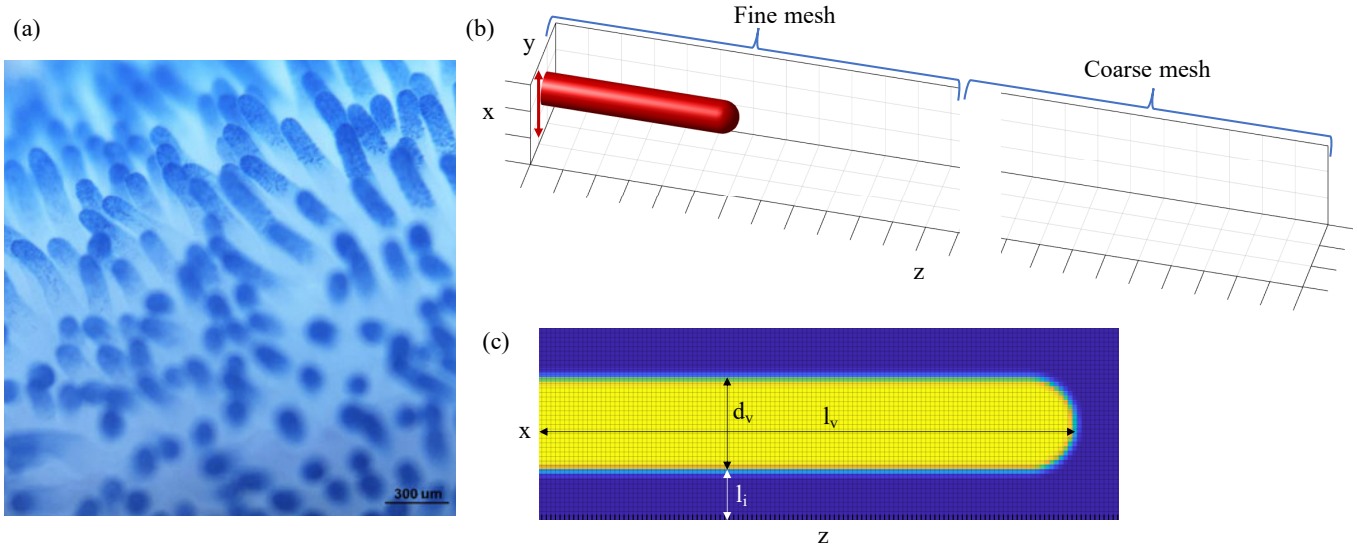

FIG. 1. **(a)** Microscopic image of villi of a mammal, adapted from[1] **(b)** Steady flow induced by an infinite array of villi which oscillated in the x direction was simulated. The computational domain was covered by a fine and a coarse mesh. Periodic boundary conditions were considered in the x and y directions. The red arrow indicates the direction of the oscillation. **(c)** The smoothed profile of a villi in the (x-z) plane. The lines are the lattice grid and the contour is the villi domain which is described by Eq.11 with $d_v = 20\Delta x$ and $\xi = \Delta x$.

drodynamical tweezers.[32] In the biological world, self-propulsion of micro-swimmers at moderate Reynolds number[33] and mixing in micro-cavities in the respiratory system (acinar)[34] have been attributed to SSF. Periodic forcing induces the emergence of an unsteady viscous boundary layer near the boundary in which the vorticity is non-zero, the so-called Stokes layer δ^{St}. Consequently, the main non-dimensionless number that characterizes SSF is the modified Reynolds number (or Womersley number), $Re_m = d\sqrt{\omega\rho/\mu}$, which represents the ratio between the characteristic length of the flow d and the thickness of the Stokes layer $\delta^{St} = \sqrt{\mu/\omega\rho}$ where μ is the fluid viscosity, ω the pulsation of the forcing, and ρ the fluid density. Concerning small intestine villi, our hypothesis is supported at first sight by the fact that the Stokes layer is of the same order of magnitude as the dimensions of the villi; $Re_m \sim 0.1 - 1$, by taking the villi diameter d_v as the characteristic length (Table I).

Our objective is to simulate steady streaming flow induced by small intestine villi in a prototypical situation and these effects on fluid transport on long time scales. We considered a 3D infinite array of oscillating villi in a semi-infinite space. For this purpose, we developed a flow solver that combined a lattice-Boltzmann model with two-relaxation times and the smoothed profile method in order to capture this second order flow phenomena. Firstly, we validated the model with a benchmark. Secondly, we studied the influence of the different dimensionless parameters on the thickness of the unsteady viscous boundary layer. Thirdly, we showed that steady-streaming flow patterns are strongly dependent on the lateral confinement between the villi. Lastly, we discussed the consequences of SSF phenomena at scale of villi on mass transfers and transport of particles in the small intestine of mammals.

TABLE I. Typical values of parameters characterizing villi geometry and the motility of small intestine in mammals, values from Refs[1,22,35,36]

Diameter of the villi	d_v	200 μm
Length of the villi	l_v	500 μm
Inter-villi space	l_i	50-250 μm
Amplitude of translation	a	150 μm
Frequency	f	0.7 Hz
Amplitude of velocity	$U_0 = 2\pi f a$	0.66 mm/s
Fluid density	ρ	10^3 kg/m^3
Fluid viscosity	μ	0.7 mPa.s
Stokes layer	$\delta^{St} = \sqrt{\frac{\mu}{2\pi f \rho}}$	400 μm
Modified Reynolds number	$Re_m = d_v/\delta^{St}$	0.5

II. MODEL AND METHODS

The three-dimensional geometry under consideration was an infinite array of small intestine villi with a finger-like structure by using periodic boundary conditions in x and y directions, Fig. 1-a, b. We considered a semi-infinite space as the length of the villi ($\sim$ 500 μm) is small compared to the diameter of the small intestine ($\sim$ 1-5 cm). In regard to experimental evidence, we considered the villi as a rigid structure.[22] Table I gives typical geo-

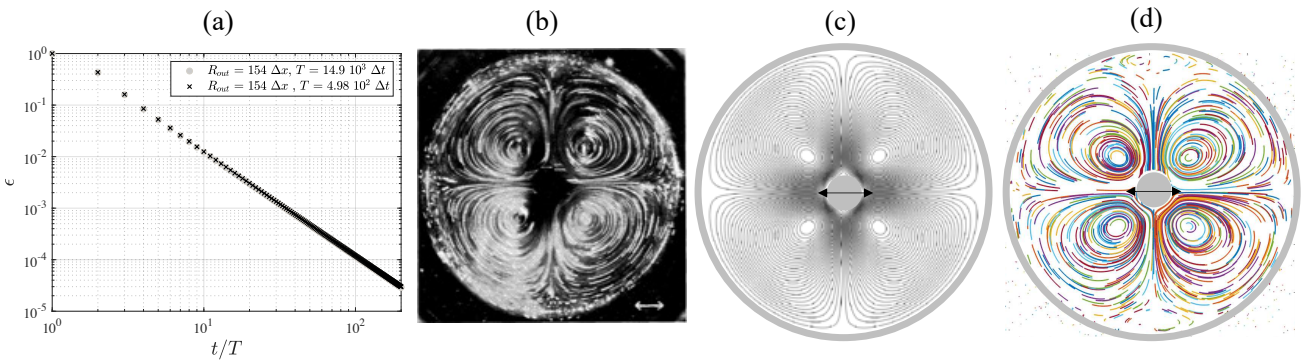

FIG. 2. Simulation of steady streaming flow in an oscillating centered annuli and comparison with experiments. **(a)** The relative error ϵ for different temporal resolutions as a function of the number of cycles. **(b)** Experimental steady Lagrangian streamlines obtained by Tatsuno[29]. The arrows show the direction of oscillation of the inner cylinder. **(c)** Steady Eulerian streamlines simulated by our SPM-TRT-LBM algorithm for the same conditions as (a). **(d)** Corresponding steady Lagrangian streamlines. For all the captions, $Re_m = 0.979$, $a/R_{in} = 0.322$ and $R_{out}/R_{in} = 7.69$.

metrical values of villi dimensions in several species.[22,37] We note l_v and d_v, the length and diameter of villi, respectively. ρ and μ are the density of the dynamic viscosity of the fluid. The distance between two adjacent villi is l_i. Due to the action of longitudinal smooth muscles,[35] we considered an oscillating translation of the villi in the x-direction. The velocity of translation of the villi is given by a sinusoidal function of frequency f and amplitude $U_0 = 2\pi f a$, where a is the amplitude of the displacement. The velocity was scaled by $2\pi f a$. We used the thickness of the Stokes layer $\delta^{St} = \sqrt{\mu/2\pi f \rho}$ as the typical length scale and δ^{St}/U_0 as the typical time scale. Consequently, the velocity of translation of the villi $\tilde{\mathbf{U}}_{\mathbf{V}}$ is given in dimensionless form by

$$\tilde{\mathbf{U}}_{\mathbf{V}}(\tilde{t}) = \cos\left(\frac{d_v}{a}\frac{1}{Re_m}\tilde{t}\right)\mathbf{e}_x \tag{1}$$

.

The dimensionless Navier-Stokes equations for incompressible laminar flows are given by

$$\frac{\partial \tilde{u}_i}{\partial \tilde{x}_i} = 0 \tag{2}$$

$$\frac{\partial \tilde{u}_i}{\partial \tilde{t}} + \tilde{u}_j\frac{\partial \tilde{u}_i}{\partial \tilde{x}_j} = -\frac{\partial \tilde{p}}{\partial \tilde{x}_i} + \frac{d_v}{a}\frac{1}{Re_m^2}\frac{\partial^2 \tilde{u}_i}{\partial \tilde{x}_j \partial \tilde{x}_j} \tag{3}$$

where i, j (=1,2,3) are the indices of the system of coordinates. $\tilde{u}_i$, $\tilde{t}$, $\tilde{x}_i$, and $\tilde{p}$ are the dimensionless velocity, time, coordinate, and pressure, respectively. Therefore, four independent variables defined our problem: the modified Reynolds number $Re_m = d_v\sqrt{2\pi f\rho/\mu}$, the reduced amplitude a/d_v, and the geometric ratios d_v/l_i and d_v/l_v.

Direct simulation of steady streaming flows requires a high accuracy. For this purpose, flow was solved by a combination of D3Q19 Two-Relaxation-Time (TRT) lattice-Boltzmann (LB) methods and the smoothed profile method to take into account the rigid body motion of the villi. Moreover, a multi-grid algorithm was used to simulate a semi-infinite space with a higher resolution in the viscous boundary layer induced by the villi movement.

A. TRT LBM scheme

The flow was simulated by the D3Q19 incompressible TRT Bhatnagar-Gross-Krook LB methods.[38,39] The nineteen discrete velocities are defined by

$$\mathbf{e}_\alpha = (0,0,0)\,, \alpha = 0$$

$$\mathbf{e}_\alpha = (\pm c,0,0)\,,(0,\pm c,0)\,,(0,0,\pm c)\,, \alpha = 1-6$$

$$\mathbf{e}_\alpha = (\pm c,\pm c,0)\,,(\pm c,0,\pm c)\,,(0,\pm c,\pm c)\,, \alpha = 7-18$$

where $c = \Delta x/\Delta t$, Δx and Δt are the lattice grid spacing and the lattice time step respectively. The evolution equation of the model is divided into two steps, the propagation,

$$f_\alpha\left(\mathbf{x}+\mathbf{e}_\alpha\Delta t, t+\Delta t\right) = \hat{f}_\alpha \tag{4}$$

and the collision,

$$\hat{f}_\alpha(\mathbf{x},t) = \frac{1}{\tau_+}\left[f_\alpha^+(\mathbf{x},t) - f_\alpha^{+,eq}(\mathbf{x},t)\right] + \frac{1}{\tau_-}\left[f_\alpha^-(\mathbf{x},t) - f_\alpha^{-,eq}(\mathbf{x},t)\right] + b_\alpha(\mathbf{x},t) \tag{5}$$

$$f_\alpha^+ = \frac{1}{2}\left(f_\alpha + f_{\bar{\alpha}}\right),\ f_\alpha^- = \frac{1}{2}\left(f_\alpha - f_{\bar{\alpha}}\right) \tag{6}$$

$$f_\alpha^{+,eq} = \frac{1}{2}\left(f_\alpha^{eq} + f_{\bar{\alpha}}^{eq}\right),\ f_\alpha^{-,eq} = \frac{1}{2}\left(f_\alpha^{eq} - f_{\bar{\alpha}}^{eq}\right) \quad (7)$$

where f_α is the density distribution function, f_α^{eq} is the equilibrium distribution function, symbols '+' and '−' refer to the symmetric and anti-symmetric part of both functions, $\bar{\alpha}$ is the opposite direction to α (i.e. $\mathbf{e}_\alpha = -\mathbf{e}_{\bar{\alpha}}$), τ_+ and τ_- are the two relaxation parameters, $\hat{f}$ is the density distribution function after collision and before propagation and $\mathbf{b}$ is a forcing term. f_α^{eq} is defined by

$$f_0^{eq} = 1 - (1-\omega_0)\frac{p}{c_s^2} + s_0(\mathbf{u}) \quad (8)$$

$$f_\alpha^{eq} = \omega_\alpha \frac{p}{c_s^2} + s_\alpha(\mathbf{u}), \alpha = 1-18 \quad (9)$$

where $\mathbf{u}$ is the velocity, p is the pressure, $s_\alpha(\mathbf{u}) = \omega_\alpha\left[3\mathbf{e}_\alpha.\mathbf{u} + 4.5\left(\mathbf{e}_\alpha.\mathbf{u}\right)^2 - 1.5\mathbf{u}^2\right]$, with the weight coefficients ω_0 =1/3, ω_{1-6} =1/18, ω_{7-18} =1/36 and $c_s = c/\sqrt{3}$ is the speed of sound. The macroscopic flow velocity and pressure are computed from the distribution functions,

$$\mathbf{u} = \sum_{\alpha=1}^{18} \mathbf{e}_\alpha f_\alpha,\ p = \frac{c_s^2}{1-\omega_0}\left[\sum_{\alpha=1}^{18} \mathbf{e}_\alpha f_\alpha + s_0(\mathbf{u})\right] \quad (10)$$

The dynamic lattice viscosity is given by $\eta = c_s^2(\tau_+ - 1/2)\Delta t$. The major interest of the TRT model compared to the Single Relaxation Time (SRT) model is to tune the lattice viscosity by changing τ_+ without loss of accuracy when the relaxation parameter is larger than 1.[38] The second relaxation parameter is defined by $\tau_- = \frac{\Lambda}{\tau_+ - 0.5} + 0.5$, where Λ is the magic collision parameter and taken to 1/4 in order to optimize the accuracy of the numerical scheme.[40] The practical implication of the TRT model for simulating steady streaming is being able to choose the physical grid resolution independently of the physical time steps, without any loss of accuracy, in order to accelerate the convergence of the simulation.

Whereas periodic boundary conditions were applied in x and y directions, no-slip boundary conditions were enforced at the top and bottom of the computational domain, i.e. $\mathbf{u}(z=0) = \mathbf{U_v}(t)$ and $\mathbf{u}(z = Z_{max}) = 0$. Preliminary tests were carried out in order to find a sufficenlty large value of Z_{max} that did not influence the results.

B. Smoothed profile method

Moving boundary conditions were enforced using the smoothed profile method (SPM), which was developed to consider multi-body hydrodynamic interactions of solid particles.[41] It has been recently combined with LBM to investigate the rheology of concentrated suspensions of rigid particles.[42] The principle is to couple the rigid body dynamics and the flow dynamics through a smoothed profile of the rigid body. This approach makes it possible to use the same lattice grid for both flow and rigid body, and the operations are local, which made the method highly efficient and easily used in parallel computing. Furthermore, describing the boundary between the fluid and the rigid body by a continuous and smoothed interface reduces the numerical errors associated with the interpolation-extrapolation methods generally used for curved and moving boundary conditions in LBM solvers.[43,44]

The profile function Φ_V of the villi was simply built as the stack of disks of diameter d_v, thickness Δx and total length l_v. The profile Φ_D of each disk is given by

$$\Phi_D(\mathbf{x}) = \frac{1}{2}\left[1 + \tanh\frac{d/2 - |\ \mathbf{x} - \mathbf{X_c}\ |}{\xi}\right] \quad (11)$$

where $\mathbf{x}$ is the position of lattice nodes, $\mathbf{X_c}$ the center of the disk and ξ the interface thickness. The tip of the villi was modeled by a semi-spherical cap. In the fluid region, $\Phi_V = 0$ while $\Phi_v = 1$ in solid villi region, and it continuously changes near the interfacial region, Fig. 1-c. In this study, $\xi = 1\Delta x$ as it is commonly used.[41,42]

No-slip boundary conditions were enforced by computing the fluid-solid interaction force at each lattice $\mathbf{x}$ by

$$\mathbf{f_V}(\mathbf{x},t) = \Phi_V(\mathbf{x},t)\left[\mathbf{U_V}(t) - \mathbf{u}(\mathbf{x},t)\right]/\Delta t \quad (12)$$

with $\mathbf{u}$ the fluid velocity computed in Eq. 10 and $\mathbf{U_V}$ the translational velocity of the villi. The latter is given by a sinusoidal function of frequency f and amplitude $U_0 = 2\pi f a$, where a is the amplitude of the displacement

$$\mathbf{U_V}(t) = U_0 \cos(2\pi f t)\,\mathbf{e}_x \quad (13)$$

The hydrodynamic force at the lattice node $\mathbf{x}$ is given by

$$\mathbf{f_H}(\mathbf{x},t) = -\mathbf{f_V}(\mathbf{x},t) \quad (14)$$

and added to the collision step (Eq. 6) via the forcing term $b_\alpha = -3\omega_\alpha \mathbf{f_H}.\mathbf{e}_\alpha$, to enforce no-slip boundary conditions.

C. Multi-grid algorithm

The communication and reconstruction of information between the two sets of grids (Fig. 1-a) were done with the coupling algorithms of Dupuis and Chopard.[45] The interest of these algorithms is to be accurate for all values of the relaxation time τ_+. In their algorithm, Dupuis and Chopard choose to keep the same velocities $\mathbf{u}$ on different lattices and so the ratio $\Delta x/\Delta t$ for the two grids, which implies that Δt changes from one grid level to the other.

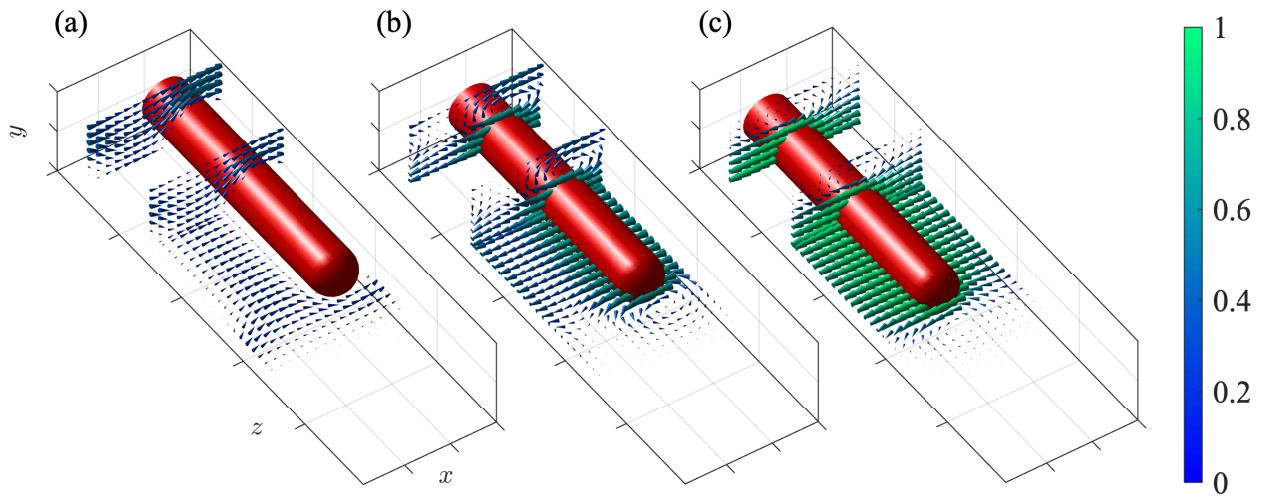

FIG. 3. Instantaneous flow at different time steps **(a)** t=0, **(b)** t=T/8 **(c)** t=T/4 and in three different planes. The color map shows the magnitude of the dimensionless velocity $|\mathbf{u}|/U_0$. $Re_m = 1$, $a/d_v = 0.5$, $l_v/d_v = 5.5$, $l_i/d_v = 1$.

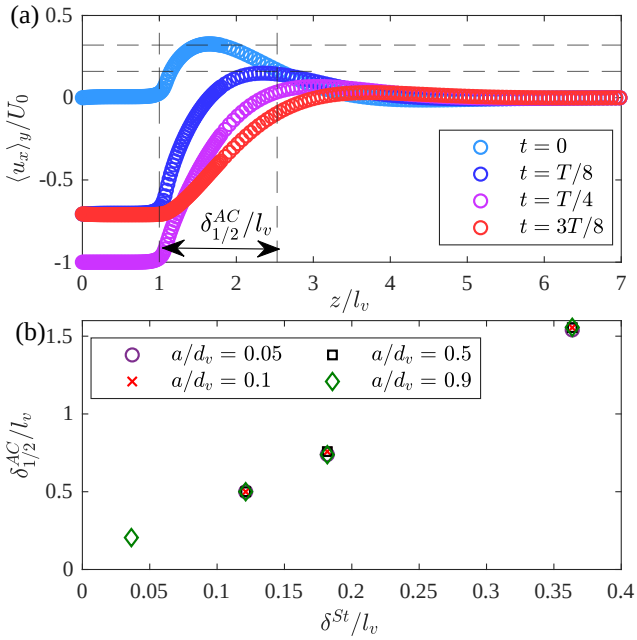

FIG. 4. The unsteady boundary layer. **(a)** Averaged velocity profile in the x direction $\langle u_x \rangle_y / U_0$ at different time steps. $\delta^{AC}_{1/2}$ is the thickness of the unsteady viscous boundary layer as defined by Eq. 19. Re_m=0.5, a/d_v=0.5, l_i/d_v=1, l_v/d_v=5.5. **(b)** Normalised unsteady boundary layer thickness $\delta^{AC}_{1/2}/l_v$ as a function of δ^{St}/l_v for different amplitudes of oscillation a/d_v.

On the other hand, this choice requires modifying the relaxation time τ_+ in order to keep the viscosity constant across the grids. Hence, the relationship between the relaxation time of the coarse and fine grids is,

$$\tau^f_+ = \frac{\Delta x^c}{\Delta x^f}\left(\tau^c_+ - \frac{1}{2}\right) + \frac{1}{2} \tag{15}$$

where subscripts 'c' and 'f' refer to the coarse and fine grids respectively. At the interface between the two grids, information has to be exchanged between fine and coarse grids at the streaming step (Eq.4). The transformation between fine and coarse grids is given by

$$f^c_\alpha = f^{f,eq}_\alpha + \left(f^f_\alpha - f^{f,eq}_\alpha\right)\frac{n\tau^c_+}{\tau^f_+} \tag{16}$$

$$f^f_\alpha = \widetilde{f}^{c,eq}_\alpha + \left(\widetilde{f}^c_\alpha - \widetilde{f}^{c,eq}_\alpha\right)\frac{\tau^f_+}{n\tau^c_+} \tag{17}$$

where $n = \Delta x^c/\Delta x^f$ and $\widetilde{f}_\alpha$ denotes the spatially and temporally interpolated value of f on the coarse grid. The reader can refer to Refs.[23,45] for validation of this specific algorithm.

D. Steady streaming flow resolution

The Eulerian steady streaming velocity field $\mathbf{u_s}(\mathbf{x})$ is the non-reversible part of the velocity field $\mathbf{u}(\mathbf{x})$. It is so defined as the mean temporal value of the velocity field in the pseudo-steady state over one cycle of activity, i.e.

$$\mathbf{u_s}(\mathbf{x}) = \frac{1}{T}\int_0^T \mathbf{u}(\mathbf{x}, t)\mathrm{d}t \tag{18}$$

with $T = 1/f$.

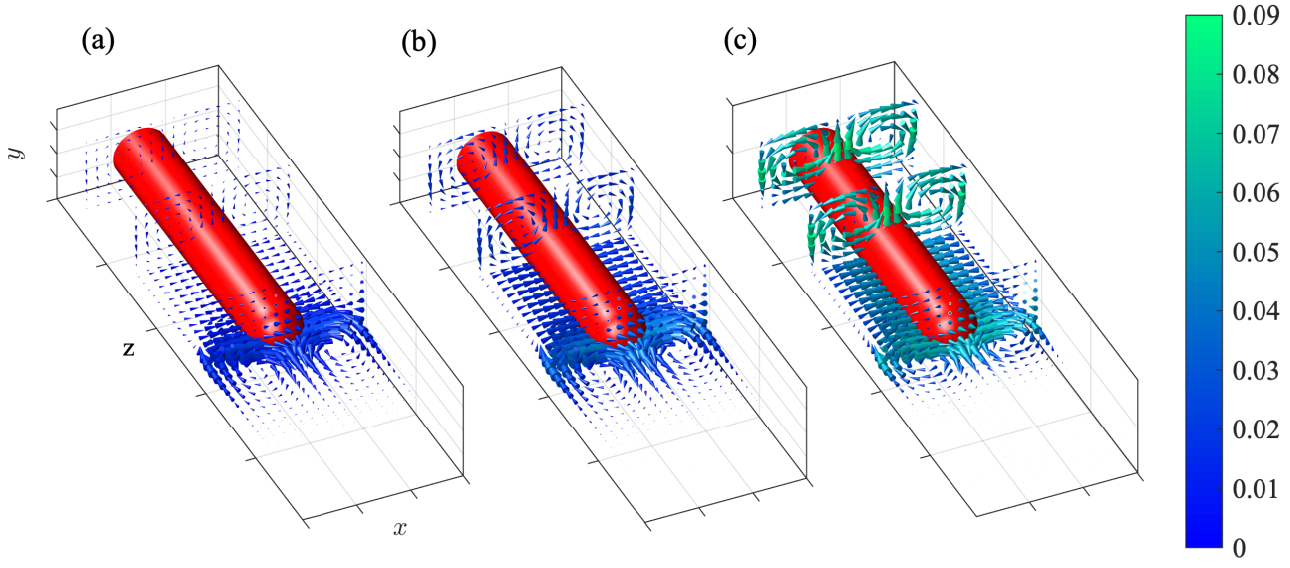

FIG. 5. Steady streaming flow patterns induced by the oscillation of a villi in the x direction for **(a)** $Re_m = 0.1$, **(b)** $Re_m = 1$ and **(c)** $Re_m = 3.5$. The color map shows the magnitude of the dimensionless steady streaming velocity $\mid \mathbf{u_s} \mid /U_0$. $a/d_v = 0.5$, $l_v/d_v = 5.5$ and $l_i/d_v = 1$.

The pseudo-steady state of the flow was achieved by convergence of the L2-norm ϵ of $\mid \mathbf{u_s}(\mathbf{x}, t+T) - \mathbf{u_s}(\mathbf{x}, t) \mid$ ($< 10^{-4}$). Typically, the small lattice grid consisted of a mesh of at least $30 \times 30 \times 100$ nodes and the size ratio n between the coarse and fine grids was at least 3. One cycle of activity was divided into at least 10^3 time steps. The Lagrangian streamlines of the SSF were computed by integrating over time, the position of markers randomly dispersed in the computational domain, i.e. $\mathbf{x}(t + \Delta t) = \mathbf{x}(t) + \mathbf{u}(t)\Delta t$, and were plotted at the end of each cycle of oscillation.

III. RESULTS

A. Steady streaming flow in an oscillating centered annuli

The streaming flow in an infinitely long centered annuli[28,29,46,47] was simulated as a benchmark to validate our SPM-TRT-LBM numerical algorithm for Re_m of the order of unity, Fig. 2. The external cylinder of radius R_{out} was fixed, whereas the inner cylinder of radius R_{in} was oscillating in the (x-y) plane. We used periodic boundary conditions in the z direction. We fixed Re_m, a/R_{in} and R_{out}/R_{in} to 0.98, 0.322 and 7.69 in order to reproduce the experimental results of Tatsuno.[29] The solution dependency with the size of the mesh and the temporal resolution was studied with $R_{out} = 154\ \Delta x$ and $T = 4.9\ 10^2$ or $14\ 10^3\ \Delta t$. The relative error ϵ decreased with the number of time steps without any divergence in both cases, Fig 2-a. The slope indicated a second order convergence with time, as expected for the LBM solver.[38–40] The experimental Lagrangian SSF streamlines were obtained by observing the displacement of particles with a stroboscopic light,[29] Fig. 2-b. With this set of parameters, one inner circulation occupied each quadrant. Fig. 2-c and d respectively show the Eulerian and Lagrangian steady streamlines simulated with our SPM-TRT-LBM algorithm. Both patterns of streamlines were similar and in very good agreement with the experiments of Tatsuno.[29]

B. Unsteady flow induced by oscillating villi

The instantaneous flow patterns generated by the translation of an infinite array of villi in a semi-infinite space was localized in an unsteady boundary layer δ^{AC}, Fig. 3, as expected for pulsatile flow at non-vanishing Reynolds number.[48] Inside this boundary layer, the flow was characterized by an unsteady vortex at the tip of the villi in the (x-z) plane, whose direction of rotation was reversed every half periods. Vortices were also localised in the intervillus space in the (x-y) plane.

In order to measure the thickness of the unsteady boundary layer, we defined the mean longitudinal velocity $\langle u_x \rangle_y$ as the mean of u_x along the y direction in the mid-plane of the flow. Fig. 4-a shows the evolution of $\langle u_x \rangle_y / U_0$ as a function of z/l_v across the fine and the coarse grids. The tip of the villi was localised at $z/l_v = 1$, the upper boundary at $z/l_v = 7$ and the transition between the both grids at $z/l_v = 1.8$. The transition between both grids was smooth and continuous and well-captured by the multi-grid algorithm.[45] $\delta^{AC}_{1/2}$ was defined such as

$$\langle u_x \rangle_y (z - l_i = \delta^{AC}_{1/2}, t = T) = U_0/2 \qquad (19)$$

As expected, $\delta^{AC}_{1/2}$ scaled with the Stokes layer δ^{St} and

did not depend on the reduced amplitude a/d_v, Fig. 4-b. Consequently, the flow was more and more confined in a thin layer of fluid adjacent to the villi tips for increasing values of $Re_m = d_v/\delta^{St}$.

C. Steady streaming flow induced by oscillating villi

The 3D patterns of SSF were similar for Re_m ranging from 0.1 to 3.5 (Fig. 5). Two symmetric vortices were present at the tip of the villi in the plane of translation (x,z). These vortices were confined in a steady boundary layer of thickness δ^{DC}. Surprisingly, we noticed that δ^{DC} was independent on the unsteady Stokes layer δ^{St}. Above these boundary layers, the remaining region was globally irrotational. According to Re_m, the magnitude of the streaming flow was from 1 to 2 orders of magnitude smaller than the amplitude of velocity of villi translation U_0. In the intervillus space, SSF was characterized by four vortical structures in the plane perpendicular to the villi (x-y plane) that fully occupied each quadrant.

The finding that the steady vortices were present at the tip of the villi was of particular interest, as they created fluid transfers between the lumen and the tip of the villi over a distance which corresponds to δ^{DC}. The flux density φ associated to this pheomenon is given by averaging the absolute value of the streaming velocity in the z direction over the plane (x-y), i.e.

$$\varphi(z) = \frac{1}{S}\int_S |u_{s,z}|\mathrm{d}x\mathrm{d}y \qquad (20)$$

where S is the surface of the computational domain in the (x-y) plane. Figures 6-a and c show the profile $\varphi(z)/U_0$ along z for various Re_m and reduced amplitude a/d_v, respectively. φ/U_0 was negligible in the intervillus space ($z/l_v < 0.8$) and was maximal above the tip of the villi (z/l_v=1.1). The maximum of the flux φ_{max} increased linearly with Re_m, for values lower than 1.6 and then started to saturate, Fig. 6-b. φ_{max} also increased linearly with a/d_v up to 0.5. Above 0.5, the increase of the flux density was more moderate, Fig. 6-d. Again, whereas the amplitude of φ depended on Re_m and a/d_v, it was surprising to observe that SSF propagated in the z direction over a distance (up to z/l_v=1.5) which did not depend on Re_m and the Stokes layer δ^{St}. Typically δ^{DC}/l_v was of 0.5 in the range of parameters investigated in Fig. 6.

D. Role of lateral confinement on steady streaming flow

The role of the lateral confinement of the villi on SSF was studied by varying the inter-villus space l_i, for different Re_m and a fixed amplitude $a/d_v = 0.5$. φ_{max}/U_0 showed a maximum for a given value of l_i/d_v which depended on Re_m (Fig. 7-a). Above this optimum, φ_{max}/U_0 decreased and tended towards a constant value.

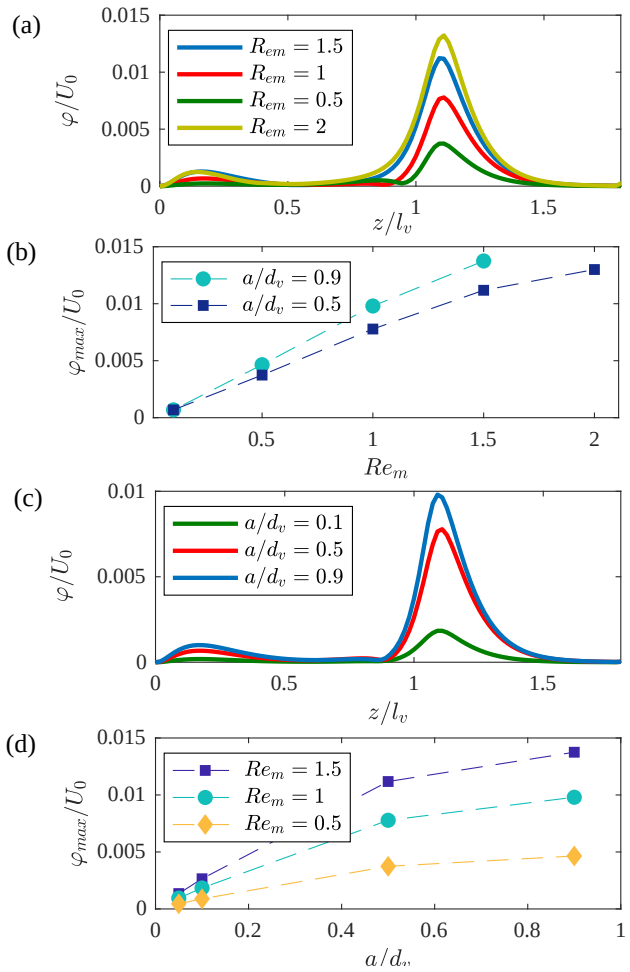

FIG. 6. Flux density φ induced by SSF in the longitudinal direction to the villi (i.e. z direction, Eq. 20). **(a)** φ profile for a fixed amplitude (a/d_v =0.5) and different Re_m. **(b)** Maximal value of φ as a function of Re_m. **(c)** φ profile for $Re_m = 1$ and different amplitudes. **(d)** Maximal value of φ as a function of a/d_v. $l_v/d_v = 5.5$ and $l_i/d_v = 1$.

This value depended also on Re_m. This set of results was rationalized by rescaling φ_{max} by $U_0 Re_m$ and the intervillus space l_i by the Stokes layer δ^{St}. Whatever the value of Re_m was, the optimum was obtained when $l_i \simeq 3\delta^{St}$. At low Re_m (< 1), the maximum of φ_{max} / $U_0 Re_m$ was constant ($\simeq 1.2\ 10^{-2}$). At larger Re_m, this value decreased. We defined the thickness of the steady boundary layer $\delta^{DC}_{1/2}$ by

$$\varphi(z - l_v = \delta^{DC}_{1/2}) = \varphi_{max}/2 \qquad (21)$$

Fig. 7-c shows that $\delta^{DC}_{1/2}/l_v$ increased with l_i/d_v. It means that the lateral confinement acted as a cut-off of the SSF above the villi. At low Re_m, the steady boundary layer reached a steady value at high l_i/d_v, whereas it continued to increase for Re_m larger than 1.5. However, this increase was not representative of the flow patterns, as explained above.

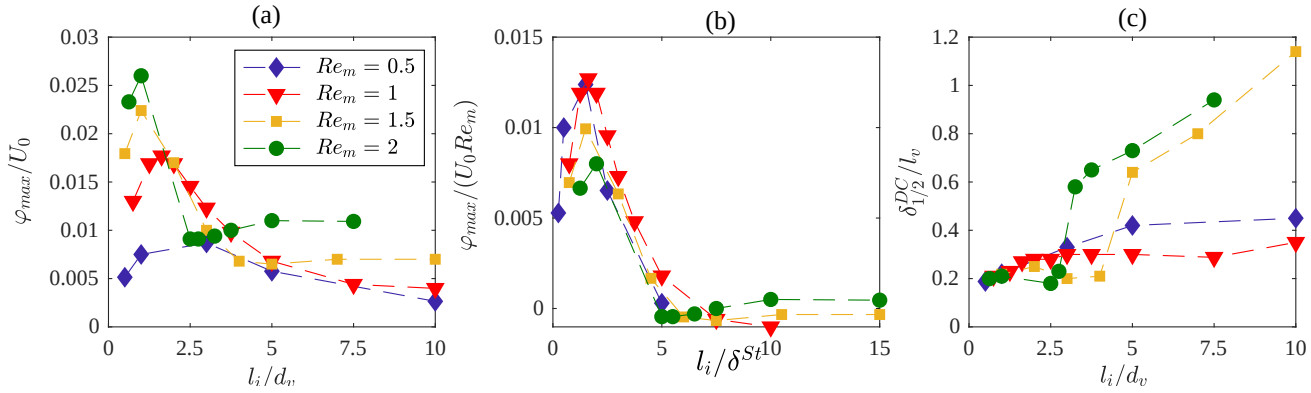

FIG. 7. Role of the lateral confinement of the villi on SSF. **(a)** Maximal flux density φ_{max} as a function of the intervillus space l_i/d_v for different Re_m. **(b)** φ_{max} was rescaled by $U_0 Re_m$ and the intervillus space l_i by the Stokes layer δ^{St}. **(c)** Steady boundary layer $\delta^{DC}_{1/2}$ as a function of l_i/d_v. $a/d_v = 0.5$, l_v/d_v =5.5.

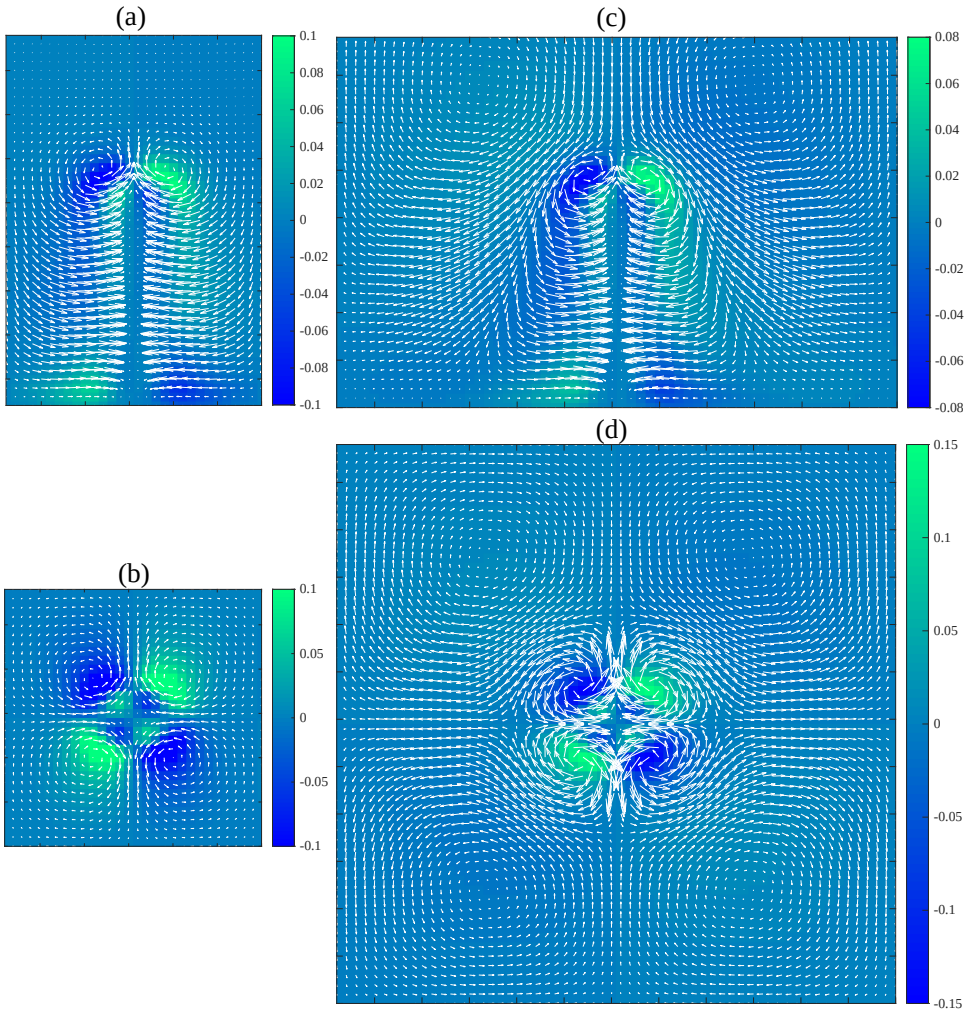

FIG. 8. Steady flow field at $Re_m = 1.5$ according to the lateral confinement of the villi in the mid-plane (top, $x - z$ plane) and at mid-height of the villi (bottom, $x - y$ plane). The color maps show the magnitude of the vorticity. **(a, b)** $l_i/\delta^{St} = 4.5$. **(c, d)** $l_i/\delta^{St} = 10.5$. $a/d_v = 0.5$, l_v/d_v =5.5. The geometrical scale is common to all figures.

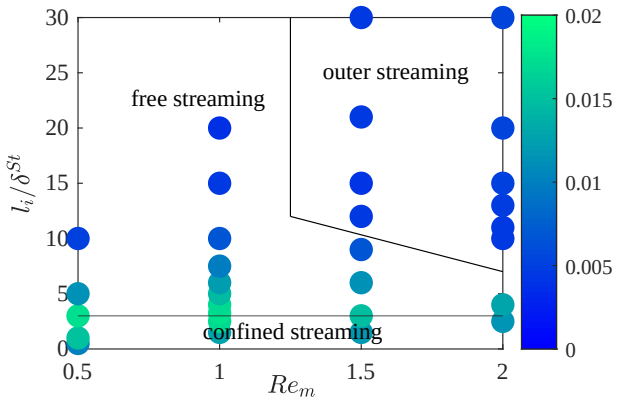

FIG. 9. State diagram of steady streaming flow patterns in the plane (Re_m-$l_i\delta^{ST}$. The color map shows φ_{max}/U_0Re_m. Below the line $l_i\delta^{ST} \simeq 3$, SSF is governed by the lateral confinement. For high $l_i\delta^{ST}$ and Re_m, outer streaming flows were observed. In the 'free streaming' region, SSF was localized in the vicinity of the villi. $a/d_v = 0.5$, l_v/d_v =5.5

Observations of the flow patterns according to the confinement allowed us to understand the mechanism at play. Fig. 8 shows flow patterns at $Re_m = 1.5$ in the cross-section of the villi in the (x,z) plane (top row) and also at the mid-height of the villi in the (x,y) plane (bottom row). Just above the optimal value of the intervillus space (l_i/δ^{St} =4.5, Fig. 8-a, b), the four vortices in the intervillus space took up the whole space. The development of the viscous boundary layer was limited by the lateral confinement, whereas at larger intervillus space (l_i/δ^{St} =10.5, Fig. 8-d), the four vortices were localized in the vicinity of the villi, and four outer vortices of lower amplitude emerged in the remaining space. The same observation was also done in the mid-plane of the villi (Fig. 8-c) where the development of the vortices at the tip of the villi was localised in the viscous boundary layer, and outer vortices emerged far from the villi. This is a consequence of the continuity of stresses between the viscous boundary layer and the remaining region, which induces an outer (Rayleigh) streaming flow. The existence of these outer vortices made artificially the value of $\delta^{DC}_{1/2}$ (Eq. 21) larger than the thickness of the steady boundary layer. It explained why the apparent thickness of the steady boundary layer, increased for Re_m larger than 1.5, in Fig. 8-c, whereas observations of the flow patterns showed that this thickness did not increased when the outer streaming was present, Fig. 7-a, c. Note that outer streaming was not observed for $Re_m < 1$ and should depend on the location of the upper boundary (i.e. Z_{max}).

IV. DISCUSSION

Inspired by small intestine villi, we numerically studied the 3D steady streaming flow forced by the reciprocal translation of an infinite array of finger-like structures (Fig. 1). We showed that such active biological microstructures are able to induce irreversible flow patterns at low, but non-vanishing Reynolds number, despite the absence symmetric forcing. Roughly, the magnitude of SSF at the tip of these microstructures was found to be almost inversely proportional to the Stokes boundary layer (Fig. 6). Consequently, the relative influence of SSF on transport and mixing cannot be generalized directly for other biological systems.

The flow patterns generated by this reciprocal forcing were mainly characterized by two symmetric vortices at the tip of the villi (Fig. 5). It was in line with the steady flow structures, which are forced by the vibration of a beam in its longitudinal direction.[27] These vortices could be responsible for mass transfers between the lumen and the tip of the villi over a distance which corresponds to the thickness of the steady boundary layer δ^{DC}. To evaluate this transfer, we defined the flux density in the direction longitudinal to the villi φ, Eq. 20. We also observed four vortices in the intervillus space (in the (x-y) plane), which are expected when a cylinder oscillates (Fig. 2).[29,46,49] Then, the effects of three main dimensionless parameters on δ^{DC} and φ were investigated: the ratio between the intervillus space l_i and the Stokes layer δ^{St}, the reduced amplitude of translation a/d_v, and the ratio between the diameter of the villi d_v and δ^{St} ($= Re_m$) .

The state diagram shown in Fig. 9 summarises our findings in the Re_m - l_i/δ^{St} space parameters for a fixed reduced amplitude $a/d_v = 0.5$. The colour code corresponds to the magnitude of φ_{max}/U_0Re_m. Three different patterns of SSF were observed that we referred to as 'confined streaming', 'free streaming' and 'outer streaming'. In the 'confined streaming' regime, the thickness of the steady boundary layer above the villi δ^{DC} was limited by the lateral confinement when the intervillus space was sufficiently small to prevent the development of the unsteady boundary layer in the intervillus space (i.e. $l_i < 3\delta^{St}$, Fig. 7-b). The SSF was optimal when the intervillus space corresponded to the unconfined steady boundary layer (Fig. 8-b, c). Above this optimal value ($l_i > 3\delta^{St}$), two situations had to be distinguished. At low Re_m, the SSF was limited to the vicinity of the villi, which is the 'free streaming' regime. The transition between 'confined' and 'free streaming' was defined at the optimum of SSF. At high Re_m and high l_i/δ^{St}, the stress induced in the steady boundary layer was sufficient to promote secondary SSF in the bulk flow (Fig. 8-c, d), which is called the Rayleigh streaming.[29] This kind of non-monotonic effect of the confinement on SSF characteristics was also reported in a bi-dimensionnal oscillating centered annuli.[46] However, it worth noting that, in the 'confined regime', the confinement in the lateral direction acted as a cut-off distance for SSF not only in the intervillus space, but also above the villi.

Having characterized SSF in a simplified geometry of small intestine villi, let us discuss their effects on mass

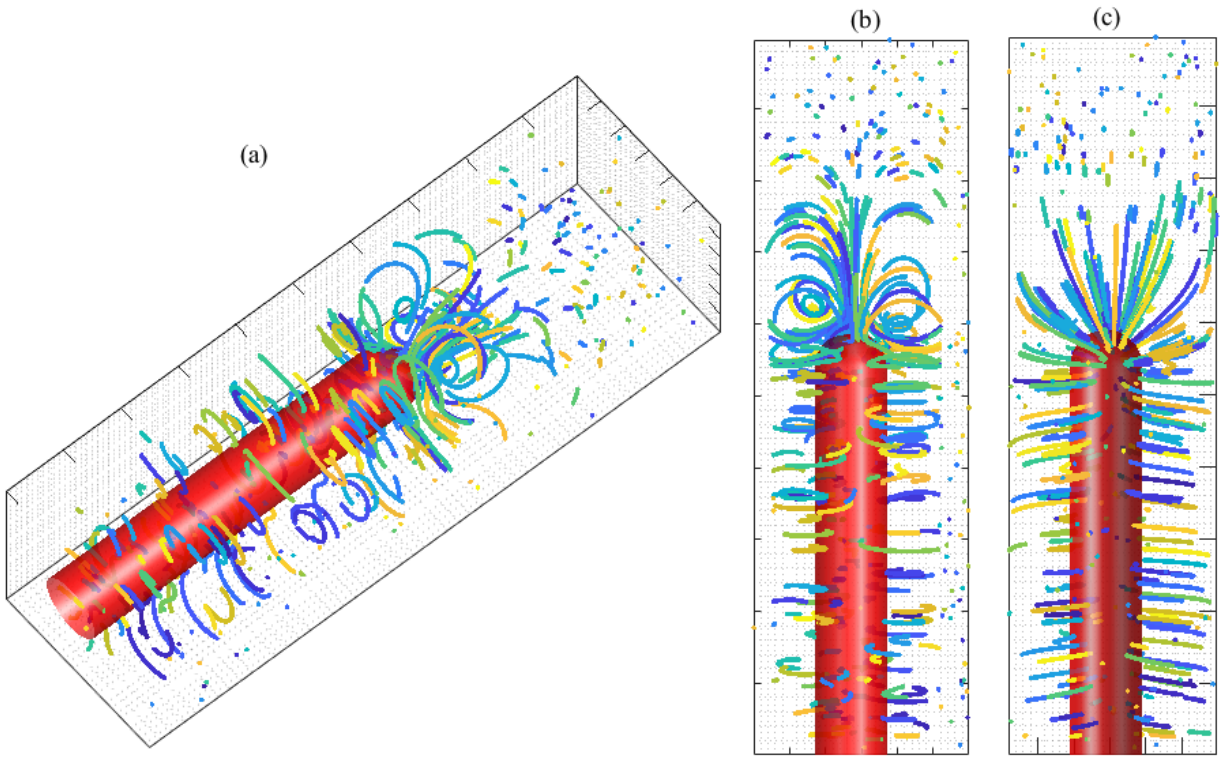

FIG. 10. Steady Lagrangian streamlines observed in **(a)** 3D, **(b)** $x-z$ plane, and **(c)** $y-z$ plane for $Re_m = 0.5$, $a/d_v = 0.5$ and l_i/d_v=2. The different colors were used to individualise the particles.

transfers in the gastrointesintal tract. Under physiological conditions, Re_m being approximately equal to 0.5 (Table I), the maximal flux density φ_{max} is of the order of 10 μm/s. For nutrients with high rates of diffusion ($D \sim 10^{-9}$ m^2/s, e.g. glucose), the associated Péclet number $Pe = \varphi_{max} d_v/D$ is lower than the unity, whereas for particles of a few dozen of nanometers ($D \sim 10^{-12}$ m^2/s), Pe is of the order of 10^3. Consequently, streaming flow phenomenon should not accelerate molecular mass transfers, but should be an important phenomena for the transport in the vicinity of the villi of nano- or micro-objects such as biliary micelles, protein aggregates, drug delivery particles or bacteria.

To support this analysis, we computed the transport of mass-less particles (i.e. the Lagrangian streamlines) at $Re_m = 0.5$ for 200 s (Fig. 10). Downward spiral movements of particles, towards the edge of the villi, were observed. Particles travelled faster at the top of the villi than in the intervillus space. The particles near the tip of the villi completed a full circular loop over a distance of a few hundred of μm; i.e. they traveled from the top to the bottom of the steady boundary layer. It is interesting to note that this time scale is long compared to the frequency of oscillation, but short in regard to the resident time of fluids in the small intestine. Therefore, SSF could be a key mechanism to transport particles near the mucosa of the small intestine. A more detailed description and modelling of this mechanism could be achieved through *ex-vivo* experiments at micro-[22,50] and macro- scales.[51,52] Moreover, numerical simulations could be done to study the coupling with flow conditions at macroscopic scales due to the spatio-temporal organization of motility patterns.[24,36,52]

In conclusion, the mechanism of steady streaming flow should contribute to the enhancement of transport of nano- or micro-particles in the vicinity of small intestine villi. Our study contributes to a better understanding of the physical conditions faced by nano drug delivery systems at the vicinity of the mucosa.[53] Moreover, in regard to the growing body of evidence that bacterial evolution and the immune response in the gastrointestinal tract are highly dependent on the competition between flow clearance and localized mixing conditions,[54–58] our results suggested that the presence of localised mixing conditions at small scales could influence the spatial organisation of microbiota and the immune response in the small intestine.

ACKNOWLEDGMENTS

LRP is part of the LabEx Tec21 (ANR-11-LABX-0030) and of the PolyNat Carnot Institute (ANR-11-CARN-007-01). The authors thank Agence Nationale de la Recherche for its financial support of the project TransportGut, ANR-21-CE45-0015.

[1]R. Lentle, P. Janssen, C. de Loubens, Y. Lim, C. Hulls, and P. Chambers, "Mucosal microfolds augment mixing at the wall of the distal ileum of the brushtail possum," Neurogastroenterology & Motility **25**, 881–e700 (2013).

[2]E. M. Purcell, "Life at low reynolds number," American journal of physics **45**, 3–11 (1977).

[3]J. O. Dabiri, "Landmarks and frontiers in biological fluid dynamics," Physical Review Fluids **4**, 110501 (2019).

[4]K. Margaris and R. A. Black, "Modelling the lymphatic system: challenges and opportunities," Journal of the Royal Society Interface **9**, 601–612 (2012).

[5]W. F. Marshall and C. Kintner, "Cilia orientation and the fluid mechanics of development," Current Opinion in Cell Biology **20**, 48–52 (2008).

[6]C. Brennen and H. Winet, "Fluid mechanics of propulsion by cilia and flagella," Annual Review of Fluid Mechanics **9**, 339–398 (1977).

[7]A. Dauptain, J. Favier, and A. Bottaro, "Hydrodynamics of ciliary propulsion," Journal of Fluids and Structures **24**, 1156–1165 (2008).

[8]B. Siyahhan, V. Knobloch, D. de Zélicourt, M. Asgari, M. Schmid Daners, D. Poulikakos, and V. Kurtcuoglu, "Flow induced by ependymal cilia dominates near-wall cerebrospinal fluid dynamics in the lateral ventricles," Journal of the Royal Society Interface **11**, 20131189 (2014).

[9]D. J. Smith, T. D. Montenegro-Johnson, and S. S. Lopes, "Symmetry-breaking cilia-driven flow in embryogenesis," Annual Review of Fluid Mechanics **51**, 105–128 (2019).

[10]E. Loiseau, S. Gsell, A. Nommick, C. Jomard, D. Gras, P. Chanez, U. D'ortona, L. Kodjabachian, J. Favier, and A. Viallat, "Active mucus–cilia hydrodynamic coupling drives self-organization of human bronchial epithelium," Nature Physics **16**, 1158–1164 (2020).

[11]K. Schulze, "Imaging and modelling of digestion in the stomach and the duodenum," Neurogastroenterology & Motility **18**, 172–183 (2006).

[12]R. Lentle and C. De Loubens, "A review of mixing and propulsion of chyme in the small intestine: fresh insights from new methods," Journal of Comparative Physiology B **185**, 369–387 (2015).

[13]A. Strocchi and M. D. Levitt, "Role of villous surface area in absorption science versus religion," Digestive Diseases and Sciences **38**, 385–387 (1993).

[14]H. Westergaard, K. Holtermuller, and J. M. Dietschy, "Measurement of resistance of barriers to solute transport in vivo in rat jejunum," American Journal of Physiology-Gastrointestinal and Liver Physiology **250**, G727–G735 (1986).

[15]D. Mailman, W. A. Womack, P. R. Kvietys, and D. N. Granger, "Villous motility and unstirred water layers in canine intestine," American Journal of Physiology-Gastrointestinal and Liver Physiology **258**, G238–G246 (1990).

[16]M. D. Levitt, A. Strocchi, and D. G. Levitt, "Human jejunal unstirred layer: evidence for extremely efficient luminal stirring," American Journal of Physiology-Gastrointestinal and Liver Physiology **262**, G593–G596 (1992).

[17]M. Gruby and M. Delafond, "Resultats des recherches faites sur l'anatomie et les fonctions des villosites intestinales, l'absorption, la preparation et la composition organique du chyle dans les animaux," CR Acad Sci **16**, 1194–1197 (1843).

[18]B. Hambleton, "Note upon the movements of the intestinal villi," American Journal of Physiology-Legacy Content **34**, 446–447 (1914).

[19]E. Kokas, "Intestinal villous motility and its regulation," The American Journal of Digestive Diseases **10**, 974–976 (1965).

[20]W. Joyner and E. Kokas, "Effect of various gastrointestinal hormones and vasoactive substances on villous motility," Comparative Biochemistry and Physiology Part A: Physiology **46**, 171–181 (1973).

[21]W. A. Womack, J. A. Barrowman, W. H. Graham, J. N. Benoit, P. R. Kvietys, and D. N. Granger, "Quantitative assessment of villous motility," American Journal of Physiology-Gastrointestinal and Liver Physiology **252**, G250–G256 (1987).

[22]Y. F. Lim, R. G. Lentle, P. W. Janssen, M. A. Williams, C. de Loubens, B. W. Mansel, and P. Chambers, "Determination of villous rigidity in the distal ileum of the possum (trichosurus vulpecula)," PloS one **9**, e100140 (2014).

[23]Y. Lim, C. de Loubens, R. Love, R. Lentle, and P. Janssen, "Flow and mixing by small intestine villi," Food & Function **6**, 1787–1795 (2015).

[24]Y. Zhang, P. Wu, R. Jeantet, D. Dupont, G. Delaplace, X. D. Chen, and J. Xiao, "How motility can enhance mass transfer and absorption in the duodenum: Taking the structure of the villi into account," Chemical Engineering Science **213**, 115406 (2020).

[25]R. G. Lentle and P. W. Janssen, *The physical processes of digestion* (Springer Science & Business Media, 2011).

[26]N. Riley, "Steady Streaming," Annual Review of Fluid Mechanics **33**, 43–65 (2001).

[27]M. Costalonga, P. Brunet, and H. Peerhossaini, "Low frequency vibration induced streaming in a hele-shaw cell," Physics of Fluids **27**, 013101 (2015).

[28]J. Holtsmark, I. Johnsen, T. Sikkeland, and S. Skavlem, "Boundary layer flow near a cylindrical obstacle in an oscillating, incompressible fluid," The Journal of the Acoustical Society of America **26**, 26–39 (1954).

[29]M. Tatsuno, "Circulatory streaming around an oscillating circular cylinder at low reynolds numbers," Journal of the Physical Society of Japan **35**, 915–920 (1973).

[30]M. Mackley and X. Ni, "Mixing and dispersion in a baffled tube for steady laminar and pulsatile flow," Chemical Engineering Science **46**, 3139–3151 (1991).

[31]B. Dincau, E. Dressaire, and A. Sauret, "Pulsatile flow in microfluidic systems," Small **16**, 1904032 (2020).

[32]A. Karimi, S. Yazdi, and A. Ardekani, "Hydrodynamic mechanisms of cell and particle trapping in microfluidics," Biomicrofluidics **7**, 021501 (2013).

[33]T. Dombrowski, S. K. Jones, G. Katsikis, A. P. S. Bhalla, B. E. Griffith, and D. Klotsa, "Transition in swimming direction in a model self-propelled inertial swimmer," Physical Review Fluids **4**, 021101 (2019).

[34]H. Kumar, M. H. Tawhai, E. A. Hoffman, and C.-L. Lin, "Steady streaming: A key mixing mechanism in low-reynolds-number acinar flows," Physics of Fluids **23**, 041902 (2011).

[35]R. Lentle, C. De Loubens, C. Hulls, P. Janssen, M. Golding, and J. Chambers, "A comparison of the organization of longitudinal and circular contractions during pendular and segmental activity in the duodenum of the rat and guinea pig," Neurogastroenterology & Motility **24**, 686–e298 (2012).

[36]C. de Loubens, R. G. Lentle, R. J. Love, C. Hulls, and P. W. Janssen, "Fluid mechanical consequences of pendular activity, segmentation and pyloric outflow in the proximal duodenum of the rat and the guinea pig," Journal of the Royal Society Interface **10**, 20130027 (2013).

[37]Y. Hosoyamada and T. Sakai, "Structural and mechanical architecture of the intestinal villi and crypts in the rat intestine: integrative reevaluation from ultrastructural analysis," Anatomy and Embryology **210**, 1–12 (2005).

[38]I. Ginzburg, F. Verhaeghe, and D. d'Humieres, "Two-relaxation-time lattice boltzmann scheme: About parametrization, velocity, pressure and mixed boundary conditions," Communications in Computational Physics **3**, 427–478 (2008).

[39]D. Rui and B.-c. Shi, "Incompressible multi-relaxation-time lattice boltzmann model in 3-d space," Journal of Hydrodynamics, Ser. B **22**, 782–787 (2010).

[40]D. d'Humières and I. Ginzburg, "Viscosity independent numerical errors for lattice boltzmann models: From recurrence equations to "magic" collision numbers," Computers & Mathematics with Applications **58**, 823–840 (2009).

[41]Y. Nakayama and R. Yamamoto, "Simulation method to resolve hydrodynamic interactions in colloidal dispersions," Physical Re-

view E **71**, 036707 (2005).
[42]S. Jafari, R. Yamamoto, and M. Rahnama, "Lattice-boltzmann method combined with smoothed-profile method for particulate suspensions," Physical Review E **83**, 026702 (2011).
[43]M. Bouzidi, M. Firdaouss, and P. Lallemand, "Momentum transfer of a boltzmann-lattice fluid with boundaries," Physics of Fluids **13**, 3452–3459 (2001).
[44]P.-H. Kao and R.-J. Yang, "An investigation into curved and moving boundary treatments in the lattice boltzmann method," Journal of Computational Physics **227**, 5671–5690 (2008).
[45]A. Dupuis and B. Chopard, "Theory and applications of an alternative lattice boltzmann grid refinement algorithm," Physical Review E **67**, 066707 (2003).
[46]A. Bertelsen, A. Svardal, and S. Tjøtta, "Nonlinear streaming effects associated with oscillating cylinders," Journal of Fluid Mechanics **59**, 493–511 (1973).
[47]K. Ilin and M. A. Sadiq, "Steady viscous flows in an annulus between two cylinders produced by vibrations of the inner cylinder," arXiv:1008.4704 (2010).
[48]C. Loudon and A. Tordesillas, "The use of the dimensionless womersley number to characterize the unsteady nature of internal flow," Journal of Theoretical Biology **191**, 63–78 (1998).
[49]B. R. Lutz, J. Chen, and D. T. Schwartz, "Microscopic steady streaming eddies created around short cylinders in a channel: Flow visualization and stokes layer scaling," Physics of Fluids **17**, 023601 (2005).
[50]S. Kuriu, N. Yamamoto, and T. Ishida, "Microfluidic device using mouse small intestinal tissue for the observation of fluidic behavior in the lumen," Micromachines **12**, 692 (2021).
[51]C. de Loubens, R. G. Lentle, C. Hulls, P. W. Janssen, R. J. Love, and J. P. Chambers, "Characterisation of mixing in the proximal duodenum of the rat during longitudinal contractions and comparison with a fluid mechanical model based on spatiotemporal motility data," PloS one **9**, e95000 (2014).
[52]R. J. A. Agbesi and N. R. Chevalier, "Flow and mixing induced by single, colinear, and colliding contractile waves in the intestine," Physical Review Fluids **7**, 043101 (2022).
[53]L. M. Ensign, R. Cone, and J. Hanes, "Oral drug delivery with polymeric nanoparticles: the gastrointestinal mucus barriers," Advanced Drug Delivery Reviews **64**, 557–570 (2012).
[54]J. Cremer, I. Segota, C.-y. Yang, M. Arnoldini, J. T. Sauls, Z. Zhang, E. Gutierrez, A. Groisman, and T. Hwa, "Effect of flow and peristaltic mixing on bacterial growth in a gut-like channel," Proceedings of the National Academy of Sciences **113**, 11414–11419 (2016).
[55]S. Labarthe, B. Polizzi, T. Phan, T. Goudon, M. Ribot, and B. Laroche, "A mathematical model to investigate the key drivers of the biogeography of the colon microbiota," Journal of Theoretical Biology **462**, 552–581 (2019).
[56]D. Hoces, M. Arnoldini, M. Diard, C. Loverdo, and E. Slack, "Growing, evolving and sticking in a flowing environment: understanding iga interactions with bacteria in the gut," Immunology **159**, 52–62 (2020).
[57]B. Waclawiková, A. Codutti, K. Alim, and S. El Aidy, "Gut microbiota-motility interregulation: insights from in vivo, ex vivo and in silico studies," Gut Microbes **14**, 1997296 (2022).
[58]D. Labavić, C. Loverdo, and A.-F. Bitbol, "Hydrodynamic flow and concentration gradients in the gut enhance neutral bacterial diversity," Proceedings of the National Academy of Sciences **119** (2022).